PUBLICATIONS OF THE ASTRONOMICAL SOCIETY OF THE PACIFIC, 112:983–995, 2000 July

Analysis of Polarized Light with NICMOS

DEAN C. HINES, GARY D. SCHMIDT, AND GLENN SCHNEIDER

Steward Observatory, University of Arizona, Tucson, AZ 85721; dhines@as.arizona.edu, gschmidt@as.arizona.edu, gschneider@as.arizona.edu

Received 1999 November 29; accepted 2000 April 7

ABSTRACT. The Near Infrared Camera and Multi-Object Spectrometer (NICMOS) aboard the *Hubble Space Telescope* (*HST*) contains optics in Cameras 1 and 2 (NIC1 and NIC2) that enable imaging polarimetry at ~ 1 and 2 μm, respectively, with unprecedented spatial detail. Preflight thermal vacuum tests revealed that the three polarizers in each camera have unique polarizing efficiencies and that the rotational orientations within each set depart from the nominal 120° intervals. To properly interpret polarimetric data obtained with these optical systems, a reduction algorithm was developed which differs from the standard approach used for ideal polarizers. We discuss this technique, its successful application to selected NICMOS observations, and the uncertainty distributions associated with three- and four-polarizer schemes. We also present information on the NICMOS instrumental polarization, the nature and origin of image artifacts in the polarized images, and suggest observational techniques for obtaining high-quality polarimetry with the instrument. With the large number of observations already taken and the exciting prospects for an extended mission with a retrofit closed-cycle turbine cooler, NICMOS will continue to produce high-resolution imaging polarimetry in the near-infrared for many years to come.

1. INTRODUCTION

Studies of polarized light have brought about profound changes in our understanding of astronomical objects, especially within the last two decades with the advent of sensitive, large-format imaging arrays such as optical CCDs and the NICMOS3 infrared arrays. Imaging of linearly polarized light from embedded young stellar objects, bipolar nebulae, and active galaxies has shown that disks of dusty gas play key roles in the birth and death of stars and can strongly influence the observed characteristics of active galaxies.

Ideally, the design of imaging polarimeters should mimic the most efficient and sensitive filter and spectropolarimeters (e.g., Serkowski 1974; Miller, Robinson, & Goodrich 1988; Schmidt, Stockman, & Smith 1992), with twin, fully modulated, complementary optical paths generated by polarizing beam splitters and dual detector areas (so-called dual-beam design). However, the realities of formatting and packaging, particularly in the context of multifunction instruments for orbiting spacecraft, often lead to compromises. A common solution for imaging polarimetry is a single rotatable polarizer or a selection from M polarizers that are insertable into the optical path feeding a single detector array. Their predefined angular orientations, and the differences in transmission and polarizing efficiency[1] among multiple polarizers, lead to special techniques for data reduction and error analysis. Here we focus on the multiple polarizer scheme common to many spacecraft polarimeters, and in particular the $M = 3$ case used for the Near Infrared Camera and Multi-Object Spectrometer (NICMOS) aboard the *Hubble Space Telescope* (*HST*). We note that a complementary polarization analysis has been presented by Sparks & Axon (1999), which includes a new technique for compensating for the bias in the uncertainty distribution inherent in polarization measurements. Herein, we present a reduction algorithm developed specifically for NICMOS polarimetry data.

Using calibration results from NICMOS preflight thermal vacuum tests and on-orbit measurements, we apply the algorithm to NICMOS data and analyze the measurement uncertainties which ensue. Some of these results have been summarized previously by Hines, Schmidt, & Lytle (1997, hereafter HSL97) and Hines (1998).

[1] Polarizer efficiency is defined as $\epsilon = (S_{\rm par} - S_{\rm perp})/(S_{\rm par} + S_{\rm perp})$, where $S_{\rm par}$ and $S_{\rm perp}$ are the respective measured signals for a polarizer oriented parallel and perpendicular to the position angle of a fully polarized beam.

2. THE POLARIMETRIC CAPABILITIES OF NICMOS

NICMOS is a second-generation axial instrument that contains three cameras with independent 256 × 256 pixel HgCdTe detector arrays held at cryogenic temperatures. The overall sensitivity range of the instrument spans 0.8–2.5 μm. Filter sets designated POLS and POLL for the two imaging cameras, NIC1 and NIC2, respectively, each provide three polarizing elements sandwiched with bandpass filters to provide high-sensitivity observations of linearly polarized light over the range 0.8–1.3 μm and 1.9–2.1 μm with diffraction-limited resolution at wavelengths of 1.0 and 1.75 μm, respectively. The original design called for the position angle of the primary axis of each polarizer (as projected onto the detector) to be offset by 120° from its neighbor and for the polarizers have identical polarizing efficiencies. While this clean concept was not strictly achieved, the reduction technique described below enables accurate polarimetry using both the short- and long-wavelength cameras over their full fields of view.

Due to a thermal short in an optical baffle between the cold well forward dome plate and the warmer vapor-cooled shield, the solid N_2 cryogen in NICMOS sublimated at a higher than expected rate, and cryogen was exhausted on 1999 January 4. However, a servicing mission currently scheduled for mid-2001 will install a closed-loop cooling system in the aft shroud of *HST* to restore the NICMOS science capabilities. Though likely operating 10–15 K warmer than with the original coolant (arrays nominally at $\sim$75 K, filters and vapor cooled shield at $\sim$120 K), the lifetime of NICMOS will be extended indefinitely. This, coupled with existing programs and archival work, assures an extended scientific impact for the instrument and, in particular, near-IR imaging polarimetry.

2.1. Thermal Vacuum Tests

Preflight thermal vacuum tests on NICMOS included an extensive characterization of the polarimetry optics. Transmission of the nonpolarimetry optics to polarized light was also measured, allowing an estimate of the maximum instrumental polarization and the sensitivity of the grisms to polarized light.

A polarizing element attached to the Calibrated InfraRed sourCE (CIRCE) provided uniform illumination of the entire field of view with light of known polarization and position angle. Polarizing efficiencies and absolute polarizer position angles (relative to the NICMOS entrance aperture) were derived for each polarizer in POLS and POLL from images obtained at 5° increments of the calibration polarizer. The same method, but without the NICMOS polarizers in place, was used to evaluate the polarization signature imparted by the mirrors that comprise the NICMOS imaging system and to characterize the sensitivity of the NIC3 grisms to polarized light. Since no differential variations across the fields of view were found as a function of CIRCE polarizer angle, the mean value across each image was used to increase the signal-to-noise ratio.

The results of these thermal vacuum tests for NIC1 and NIC2 are shown in Figures 1 and 2, respectively. Primary findings include the following:

1. Each polarizer in each camera has a unique polarizing efficiency, with POL120S having the lowest at $\epsilon_{\rm POL120S} = 48\%$.

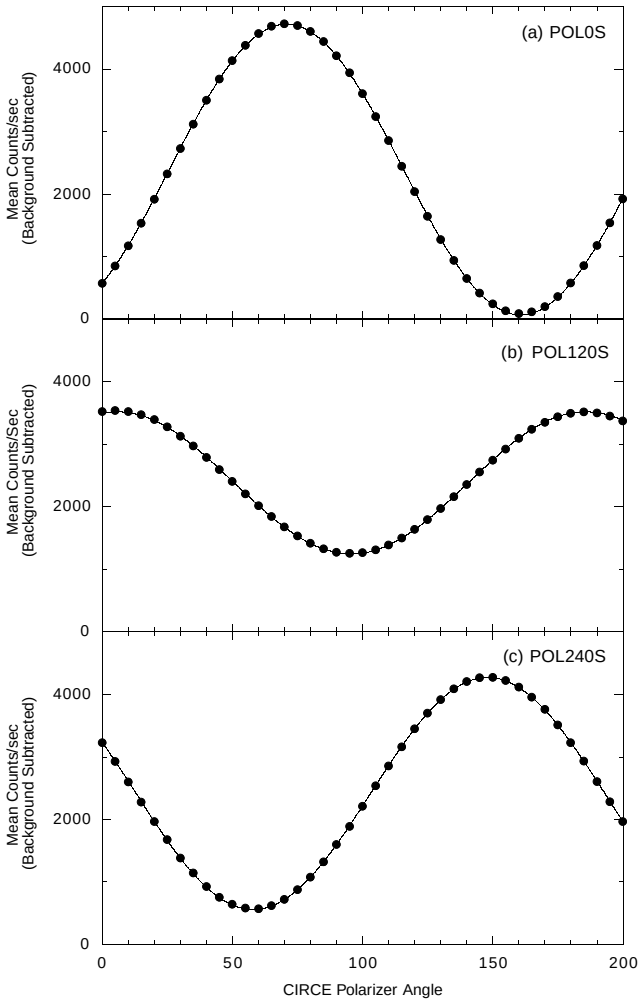

FIG. 1.—Thermal vacuum determination of polarizer orientation and polarizing efficiency for the NIC1 polarizers: (*a*) POL0S, (*b*) POL120S, (*c*) POL240S. The intensity variations of the polarizers are fit to sinusoids, from which are determined the polarizing efficiency ϵ and orientation φ (see § 3 and Table 1). Note that the CIRCE polarizer was assumed to have unity polarizing efficiency and was oriented with a 7°.67 position angle offset to the NICMOS entrance aperture. The fits yield uncertainties of $\lesssim$1% in ϵ and $\lesssim$0°.05 in φ.

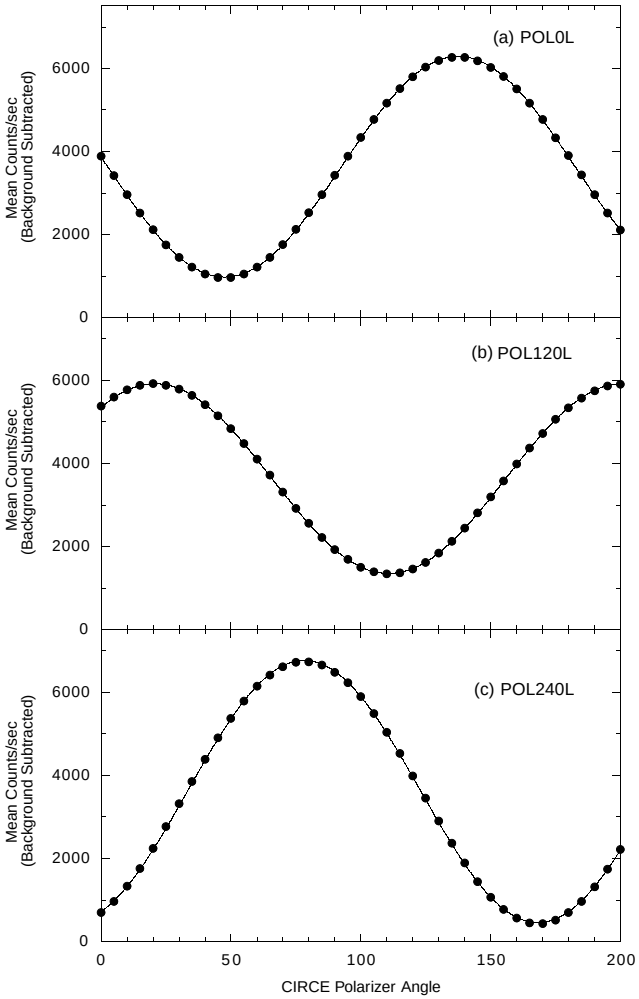

FIG. 2.—As in Fig. 1 for the polarizers in NIC2

2. Angular offsets between the polarizers within each filter wheel differ from their nominal values of 120°.

3. Instrumental polarization caused by reflections off the mirrors in the optical train is small ($\lesssim 1\%$).

4. The grisms act as partial linear polarizers, with G206 producing the largest variation in intensity ($\sim 5\%$) for completely polarized light. Because the grisms reside in the NIC3 filter wheel, they cannot be used with either the NIC1 or NIC2 polarizers and are unsuitable for spectropolarimetry.

3. AN ALGORITHM FOR REDUCING NICMOS POLARIMETRY OBSERVATIONS

At any pixel in an image, the observed signal from a polarized source of total intensity I and linear Stokes parameters Q and U measured through the kth polarizer oriented at position angle[2] φ_k is

$$S_k = A_k I + \epsilon_k (B_k Q + C_k U) . \quad (1)$$

Here

$$A_k = \frac{t_k}{2}(1 + l_k) , \quad B_k = A_k \cos 2\varphi_k ,$$
$$C_k = A_k \sin 2\varphi_k , \quad (2)$$

where ϵ_k is the polarizing efficiency, t_k is the fraction of light transmitted through the polarizer for a 100% polarized input aligned with the polarizer axis, and l_k is the "leak"—the fraction of light transmitted through the polarizer (exclusive of that involved in t_k) when the incident beam is polarized perpendicular to the axis of the polarizer. These quantities are related under the above definitions, $\epsilon_k = (1 - l_k)/(1 + l_k)$.

The equations above represent a necessary extension of the "ideal"[3] three-polarizer setup assumed in the original NICMOS Instrument Handbook (Axon et al. 1996) for the case where polarizers have individual efficiencies and angular offsets.[4] For brevity, herein we will refer to the characterization outlined above as the HSL algorithm. However, we stress that this treatment can be shown to be equivalent to other approaches, once appropriate transformations are made (Mazzuca, Sparks, & Axon 1998). Further details of the matrix inversion of a general three-polarizer system and associated covariance matrix are provided in Sparks & Axon (1999).

The values of t_k were determined initially by the filter manufacturer and were not accurately remeasured in thermal vacuum tests (HSL97). However, refinement was possible through the use of on-orbit observations of the unpolarized and polarized standard stars described in § 4. Adopted characteristics of the individual polarizers are listed in Table 1 together with the resulting coefficients of equation (1).

After solving the system of equations (eq. [1]) for the Stokes parameters at each pixel (I, Q, U), the percentage polarization (p) and position angle (θ) are calculated in the standard way:

$$p = 100\% \times \frac{\sqrt{Q^2 + U^2}}{I} , \quad \theta = \frac{1}{2}\tan^{-1}\left(\frac{U}{Q}\right) . \quad (3)$$

[2] Polarizer position angle as measured from the NICMOS Aperture Offset Angle of 224.°503, about the aperture center toward the +U3 axis.

[3] In this paper, an "ideal" M-polarizer scheme would utilize identical polarizers with unity efficiency and angular separations which are multiples of $180°/M$.

[4] Version 3.0 of the NICMOS Instrument Handbook (Calzetti et al. 1999) and Version 4.0 of the NICMOS Data Handbook (Dickinson et al. 1999) include the results of our calibration and reduction algorithm.

TABLE 1

CHARACTERISTICS OF THE NICMOS POLARIZERS AND COEFFICIENTS TO EQUATION (1)

Filter	φ_k[a]	ϵ_k	t_k[b]	l_k	A_k	$\epsilon_k B_k$	$\epsilon_k C_k$	Comments[c]
POL0S.....	1.42	0.9717	0.7760	0.0144	+0.3936	+0.3820	+0.0189	Ghosts
POL120S.....	116.30	0.4771	0.5946	0.3540	+0.4025	−0.1166	−0.1526	Weak ghosts
POL240S.....	258.72	0.7682	0.7169	0.1311	+0.4054	−0.2876	+0.1195	Ghosts
POL0L	8.84	0.7313	0.8981	0.1552	+0.5187	+0.3614	+0.1152	
POL120L.....	131.42	0.6288	0.8551	0.2279	+0.5250	−0.0411	−0.3276	
POL240L.....	248.18	0.8738	0.9667	0.0673	+0.5159	−0.3262	+0.3111	

[a] As measured from the NICMOS aperture 224°.503 about the +U3 axis.

[b] Derived from on-orbit observations of the unpolarized standard star BD +32°3739 (Schmidt, Elston, & Lupie 1992).

[c] See § 4 and Table 3.

Note that a 360° arctangent function is assumed.

This algorithm has been tested by the NICMOS Instrument Definition Team (IDT) and by the Space Telescope Science Institute (STScI) on several data sets. An implementation has been developed by the IDT and integrated into a software package written in IDL. The package is available through the STScI Web site[5] and is described by Mazzuca & Hines (1999).

4. ON-ORBIT CALIBRATION

Observations of a polarized star (CHA-DC-F7: Whittet et al. 1992) and an unpolarized (null) standard (BD +32°3739: Schmidt, Elston, & Lupie 1992) were obtained with NIC1 and NIC2 (Cycle 7 CAL 7692, 7958: Axon PI). Two epochs of data were obtained such that the differential telescope roll between observations was ∼135°. The second-epoch observations used a four-position, "spiral-dither" pattern with 20.5 pixel (NIC1) and 30.5 pixel (NIC2) offsets to improve sampling and alleviate the effects of bad pixels, cosmic rays, some persistence, and other image artifacts. While no dither pattern was used during the first epoch, the data do not appear to suffer significantly from persistence.

Since the thermal vacuum tests showed that the imaging optics themselves had little effect on the observed polarization, any measured polarization in the null standard was attributed the t_k term in the algorithm. Applying our refined coefficients to the polarized star data yielded a measured percentage polarization within 0.3% of the published value. Table 2 presents the results.

4.1. Image Ghosts in NIC1 Polarizers

During the Early Release Observations of the bright, dust-enshrouded star IRC +10216 (ERO 7120: Skinner PI), patterns of image ghosts were noted in the POL0S and POL240S observations (i.e., the NIC1 polarizers). Subsequent General Observer (GO) images of CIT 6 (GO 7548: Schmidt PI) at three different epochs revealed that the effect is also present, albeit more weakly, in the POL120S filter and that the patterns are fixed to the detector (not spacecraft) geometry.

The ghost patterns for the three short-wavelength polarizers are evident in the images of CIT 6 shown in Figure 3. Clearly, each pattern is unique in the separation, orientation, and brightness decrement of successive images (Table 3). Because the first ghost is always less than 1% the brightness of the primary image, the effect is not evident except in association with well-exposed point sources. However, the brightness decrement between successive ghosts is much flatter, a factor of 0.06–0.20, in each of the four orders of the phenomenon that can be recognized in the POL240S image. Although the ghosts evident in Figure 3 are basically faint versions of the complicated *HST*/NICMOS point-spread function (PSF), it is clear upon careful inspection that there are subtle differences in structure between the various polarizers and from one ghost to the next for a

TABLE 2

POLARIZATION MEASUREMENTS OF CHA-DC-F7

Wave Band	p (%)	σ_p[a] (%)	θ (deg)	σ_θ[a] (deg)
J (ground)[b,c]	3.19	0.05	118	2
1 μm (epoch 1).....	3.44	0.5	111	4
1 μm (epoch 2).....	3.31	0.5	108	4
K (ground)[b,c]	1.19	0.01	126	4
2 μm (epoch 1).....	0.97	0.2	119	6
2 μm (epoch 2).....	1.00	0.2	119	6

[a] No correction has been made to account for the differences between the ground-based J and K and the NICMOS POLS and POLL bandpasses.

[b] Conservative uncertainty estimates were obtained from the dispersion in results of individual "dither" positions at each epoch.

[c] Whittet et al. 1992.

[5] http://www.stsci.edu/instruments/nicmos/ISREPORTS/isr_99_004.pdf.

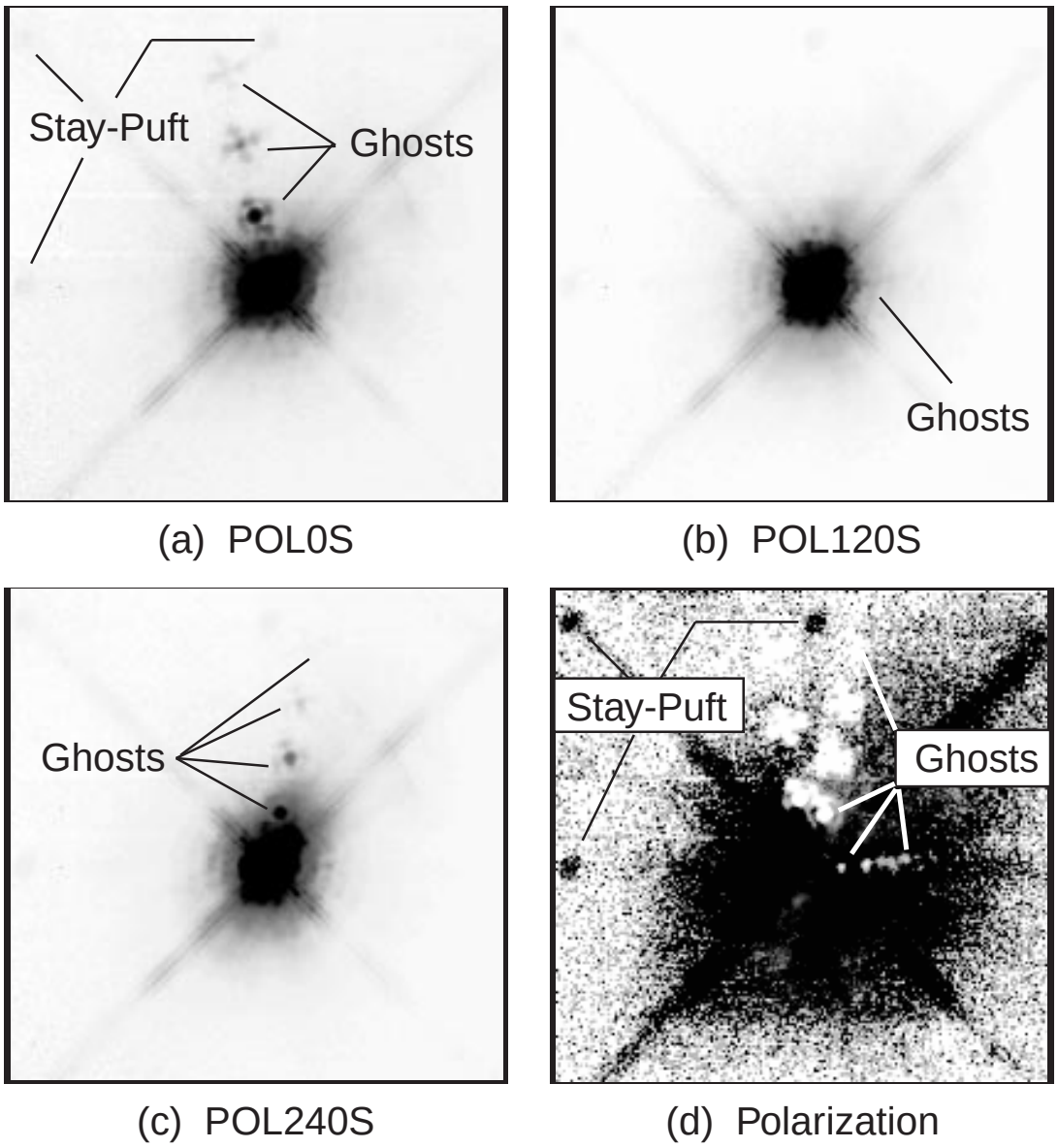

FIG. 3.—Ghost images in NIC1 polarizers: (*a*) POL0S, (*b*) POL120S, (*c*) POL240S. The gray scale in (*d*) shows the resulting percentage polarization from black ($p \leq 40\%$) to white ($p = 100\%$). Ghosts are seen as white regions that correspond with the ghost features of the three polarizer images (*a*, *b*, and *c*). The electronic "Mr. Stay-Puft" features are also indicated. Note that the ghosts have different position angles relative to the $+y$-axis of the array, which produces a strong polarization signal (see text).

given polarizer. Also notable at the left, top, and upper left in Figure 3 are the "Mr. Stay-Puft" artifacts at separations of (−128, 0), (−128, +128), and (0, +128) pixels from the bright point source. These are strictly electronic in nature.[6]

The nature of the POLS ghosts clearly suggests multiple reflections by one or more components of the NICMOS optical train that are tilted with respect to the principal ray. The facts that the pattern scale and orientations are peculiar to each polarizer of the set and that features of similar character and magnitude are not observed for any other NICMOS filters lead us to seek an origin in the construction of the polarizers themselves. These facts also rule out the possibility that the implied tilt is caused solely by the postlaunch dewar deformation that occurred during expansion of the solid nitrogen cryogen.

Each polarizer in the POLS set is a sandwich of a Polarcor™ polarizer[7] and an interference bandpass filter, spaced by a thin washer. The filters are the final optical elements in

[6] See http://www.stsci.edu/instruments/nicmos/anom_staypuft.html.

[7] Polarcor is a registered trademark of Corning, Inc.

TABLE 3

IMAGE GHOSTS IN THE POLS FILTER SET

Polarizer	Separation (pixels)	P.A.[a] (deg)	Ghost Brightness[b] ($\times 10^{-5}$)
POL0	37.8	101.7	400, 62, 7.1
POL120.....	13.7	15.7	150, 9:[c]
POL240.....	28.7	79.6	330, 70, 17, 4.5

[a] Position angle measured counterclockwise from $+x$-axis.

[b] Relative to primary image of point source.

[c] Amplitude of third-order ghost is too small to measured directly from POL120S image but is apparent in polarization image (Figs. 3*b* and 3*d*).

the converging beam, situated $\sim$440 mm ahead of the detectors. Extinction by the polarizers is nominally by absorption in a film of elongated, aligned silver grains rather than by reflection. The bandpass filters are efficient on-band, but their out-of-band reflectance is very high. We therefore envision the image ghosts to be produced by multiple reflections of largely out-of-band light within the filter-polarizer gap, with a slight wedge existing between the two components. For a wedge angle δ, such a process produces a sequence of beams which deviate by 2δ, 4δ, 6δ, ..., from the principal ray. In the geometry of the NICMOS dewar, a ghost separation of 1 mm (25 pixels) in the focal plane requires a wedge angle of $\delta \approx 4'$, or a thickness variation of $\sim$10 μm across the 11 mm diameter washer which separates the two components.

The relative brightness of the ghosts deserves some comment. In typical (achromatic) examples, images produced by multiple reflections show a uniform brightness decrement, $I_1/I_0 = I_2/I_1$, ... While this is very nearly true for adjacent ghosts of a particular POLS polarizer, a far larger decrement exists between the primary image and first ghost (Table 3). The explanation is found in the fact that one of the optical elements involved is an interference filter, which has very high reflectance outside the passband. While the principal image is almost exclusively due to on-band light, the ghosts result primarily from out-of-band light reflected within the filter gap. Thus, the brightness ratio of the principal image to the first ghost is dominated by the blocking characteristics of the filter, which is very high. Thereafter, the brightness decrement between successive ghost images bespeaks the product of the combined reflectance of the filter and polarizer to out-of-band light, and the decrement is nearly constant from one image to the next. The fact that each ghost is likely the combination of PSFs from a variety of wavelengths both above and below the passband, and therefore depends on the spectral energy distribution of the object, also explains their unique appearance.

Because the ghost patterns have different scales and orientations for the three polarizers, they can produce regions with $p \geq 100\%$ in polarization maps and are relatively easy to identify. Unfortunately, the effects are more difficult to remove. The ghosts not only result from an (unknown) polychromatic spectral energy distribution, but they exhibit progressive "softening" due to the increased optical path length, and they are subject to increased astigmatism and coma. Thus, PSF modeling is not likely to be effective. The technique of combining data from various roll angles of the spacecraft is perhaps most promising. However, we have found that even this method is problematic due to temporal changes in the PSF structure and scale of the ghost pattern arising from focal length changes in the Optical Telescope Assembly over the year-long span of our CIT 6 observations. In the worst case, the combined effects of ghosts in the three POLS filters might render up to 20% of a field useless for polarimetry.

It is important to note that the refurbished NICMOS will operate at temperatures different than those during the nominal mission in which all of the data herein were obtained. In particular, the filters and polarizers will be warmer. This could affect the gap spacing between the Polarcor and the bandpass interference filter. Therefore, after the refurbishment, the locations and detailed shapes of the ghost images may differ from those reported herein. Observations of very bright point sources (e.g., IRC +10216 and CIT 6) will be needed to evaluate these changes.

Thus far, analogous artifacts have not been recognized in POLL (NIC2: 2 μm) observations. This is possibly due to the use of more modern Polarcor elements and/or the spectral characteristics of the long-wavelength filters.

5. SCIENCE APPLICATION: IRC +10216 AND CRL 2688

Polarimetry data of known sources of extended polarized emission were obtained during the NICMOS Early Release Observations program to demonstrate the functionality of the system. Figure 4 compares the NICMOS polarimetry results for IRC +10216 (HSL97; Hines 1998; Bobrowsky et al. 2000) with the ground-based data from Kastner & Weintraub (1994). The polarization map derived by processing the NICMOS data with the HSL algorithm agrees well with the general character of the ground-based data. Both observations reveal a centrosymmetric polarization pattern centered on the strong central source. The arrow in Figure 4*b* marks the location of a polarization "feature" caused by the image ghosts in NIC1 (§ 4.1; Fig. 3). Variations of the percentage polarization in relatively uniform regions of the HSL-reduced IRC +10216 data suggest uncertainties $\sigma_{p,\,\mathrm{meas}} \lesssim 1\%$–$3\%$ (in percentage polarization per pixel), and comparison with the ground-based data suggests an uncertainty in the position angles of $\sim 2^\circ$ in 5×5 pixel bins.

Polarimetry data were also obtained for CRL 2688 with NIC2 as part of the NICMOS Early Release Observations

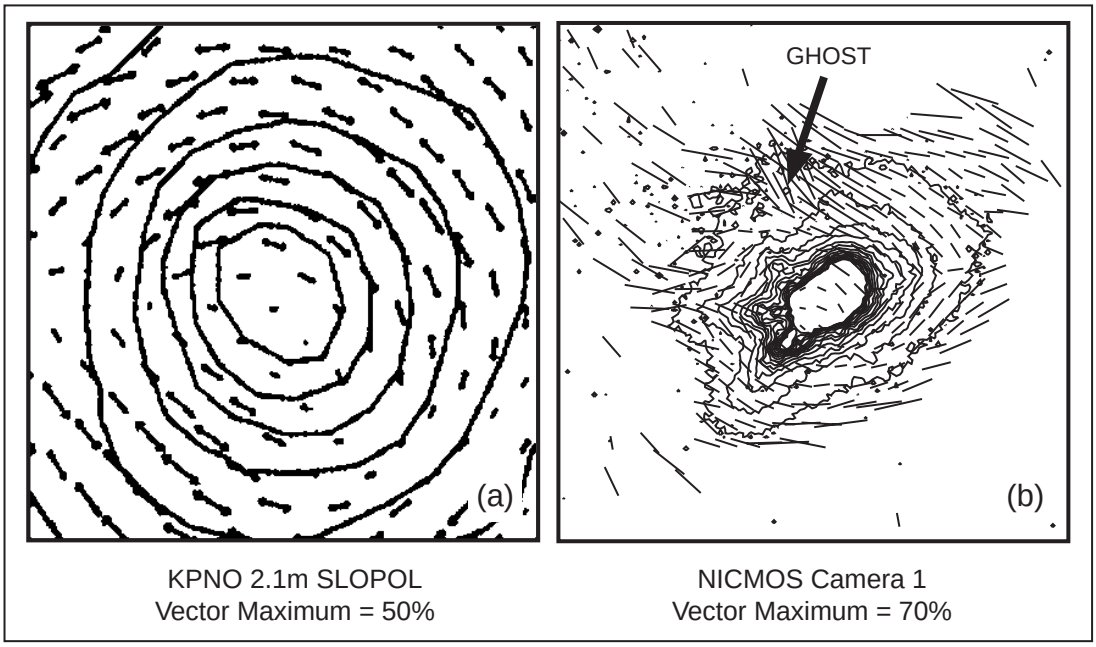

FIG. 4.—(After HSL97; Hines 1998) J-band imaging polarimetry of IRC +10216 observed from the ground (Kastner & Weintraub 1994) compared with data obtained using NICMOS Camera 1 (ERO 7120: Skinner, PI) and reduced with the HSL algorithm. For clarity, the NICMOS polarization pseudovectors are plotted for 5 × 5 pixel bins, and the faintest and brightest intensity contours have been omitted. The arrow marks the location of a polarization artifact caused by the image ghosts in the NIC1 polarizers (§ 4.1).

program (ERO 7115: Hines PI) and later with NIC1 as part of a follow-up GO program (GO 7423: Sahai PI). Combined with H_2 and WFPC2 images from associated programs, Sahai et al. (1998) presented spectacular, high-resolution renditions of the interaction between a stellar outflow and surrounding bipolar cocoon. Lacking a bright point source, the images are apparently free from ghosts. Figure 5 compares the NICMOS polarimetry results for CRL 2688 as reduced using the HSL algorithm with observations obtained from the ground and kindly provided by J. Kastner. The ground-based data are of exceptional quality and allow detailed comparison. As discussed by Sahai et al., the two data sets agree very well once the NICMOS data are binned to comparable spatial resolution, confirming that the NICMOS observations are accurately calibrated. At the full NICMOS resolution, there can be identified arcs and filamentary structures in the scattered light which reach $p = 70\%$–80%. In addition, departures from a centrosymmetric pattern of electric vectors in the interior of the reflection nebula indicate that, in addition to the post–asymptotic giant branch star, significant illumination is provided by the circumstellar disk at 2 μm.

Figure 6 shows the polarization results for CRL 2688 obtained with NIC1. We show an image of the polarization position angle to illustrate the fine detail afforded by NIC1 and because calibration errors manifest themselves most notably in position angle images (cf. Fig. 7). Although the NIC1 data are of higher spatial resolution, the measured polarization and position angle compares very favorably with the NIC2 data. This is due in part to the lack of strong point sources. The excellent agreement between the NIC1 and NIC2 results confirms that accurate, high spatial resolution polarimetry is possible with NIC1.

From this data set, we can also illustrate the effects of nonideal polarizers. Figure 7 compares the results obtained using the "standard theory" reduction assuming ideal polarizers (e.g., Axon et al. 1996) with those obtained using the HSL algorithm. The discrepancy is quite noticeable for NIC1, especially in the position angle structure. Also, the assumption of ideal polarizers seriously undermeasures the degree of polarization, ~20%–30% (Fig. 5*a*) compared with 50%–70% (Fig. 5*b*). The differences are more subtle for NIC2. In this case, the measured degree of polarization is comparable in the two methods, but the position angles are skewed in the data reduced using the standard method (Fig. 7*c*).

The CRL 2688 results attest to the polarimetric capabilities of NICMOS to accuracies of better than $\sigma_p \sim 1\%$–3% and $\sigma_\theta \sim 2^\circ$ in binned pixels (e.g., Sahai et al. 1998). Further analysis of the CRL 2688 data by Weintraub et al. (2000) using data processed with the most up-to-date NIC2 coefficients in the HSL algorithm (herein) revealed a possible 2° systematic offset in position angles based on the distribution of the relative position angles in the two lobes. However, this apparent rotation is almost certainly caused by the nonsquare projection of the pixels on the sky

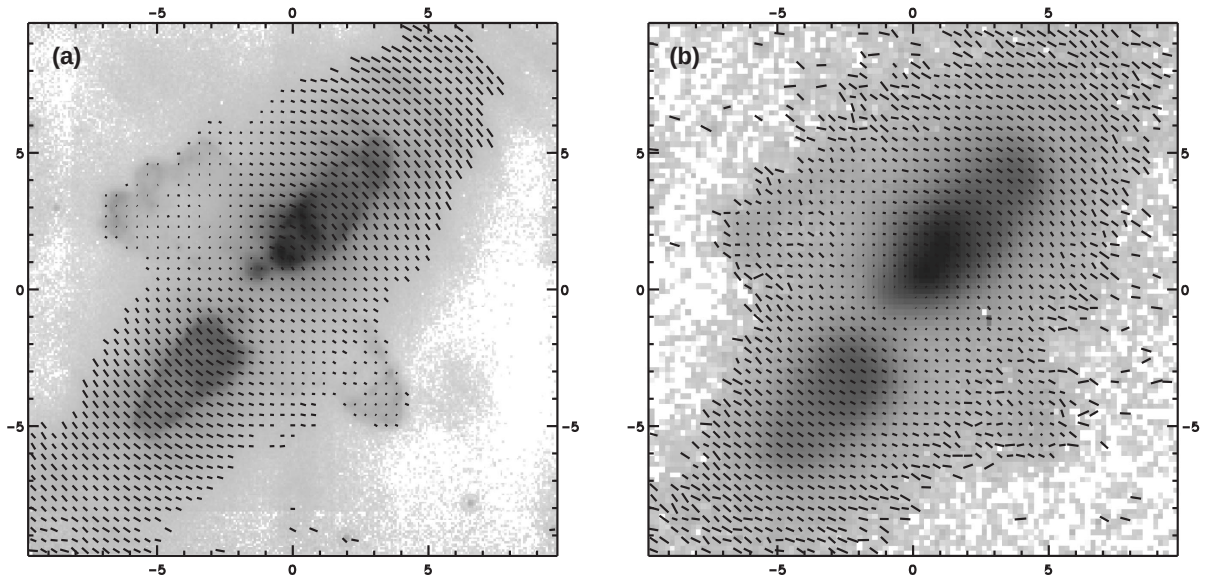

FIG. 5.—2 μm imaging polarimetry of CRL 2688 (the Egg Nebula) using (*a*) NICMOS Camera 2 (after HSL97) and (*b*) the Cryogenic Optical Bench (COB) attached to the 2.1 m telescope of Kitt Peak National Observatory (courtesy of J. Kastner). For clarity, the pseudovectors in the NICMOS and COB data are binned by 5 × 5 and 4 × 4 pixels, respectively. These data have also been presented by Sahai et al. (1998) and Weintraub et al. (2000). Geometric rectification has not been applied to the NICMOS image (see text).

(Thompson et al. 1998), and the skew can be removed by careful rectification.

We note that this effect is most important for objects whose structure lies along the diagonal of the array, as for the Egg Nebula observations. For NIC1 the projection of the pixels on the sky is closer to a square, so the maximum offset in unrectified images would be less than 1°. A more extensive discussion of the uncertainties associated

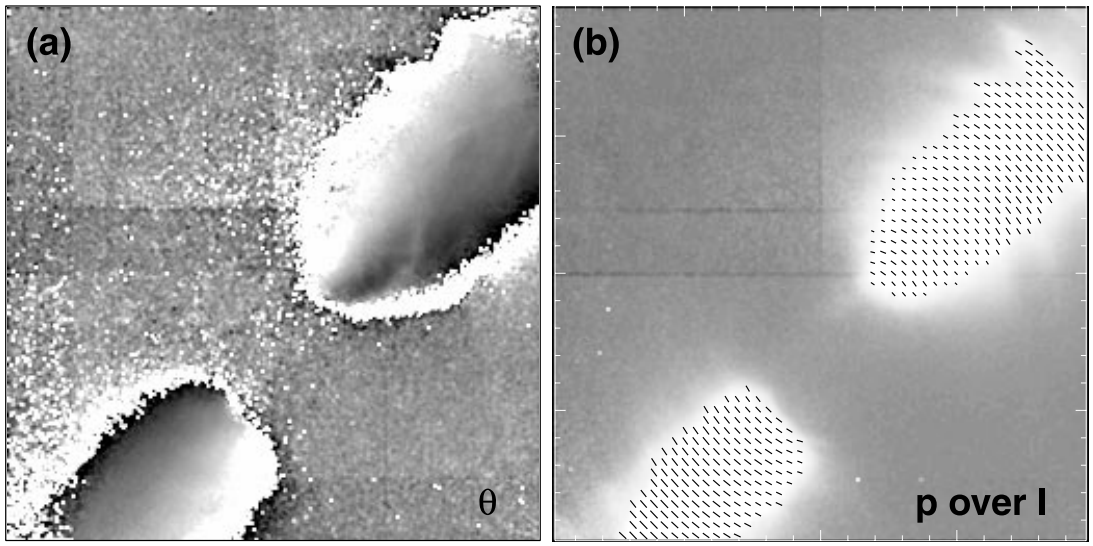

FIG. 6.—1 μm imaging polarimetry of CRL 2688 (the Egg Nebula) using NICMOS Camera 1: (*a*) the polarization position angle θ displayed from 0° to 180° (*white to black*); (*b*) the polarization pseudovectors plotted in 5 × 5 pixel bins, plotted over the total intensity image. The longest polarization pseudovectors represent 80% polarization. Note the centrosymmetric pattern typical of bipolar reflection nebulae. The detailed agreement with the 2 μm NICMOS and ground-based polarimetry (Fig. 5) confirms that the NIC1 system is capable of accurate polarimetry. CRL 2688 is not affected adversely by the ghosts shown in Fig. 3, because there are no strong point sources. Geometric rectification has not been applied to these images (see text).

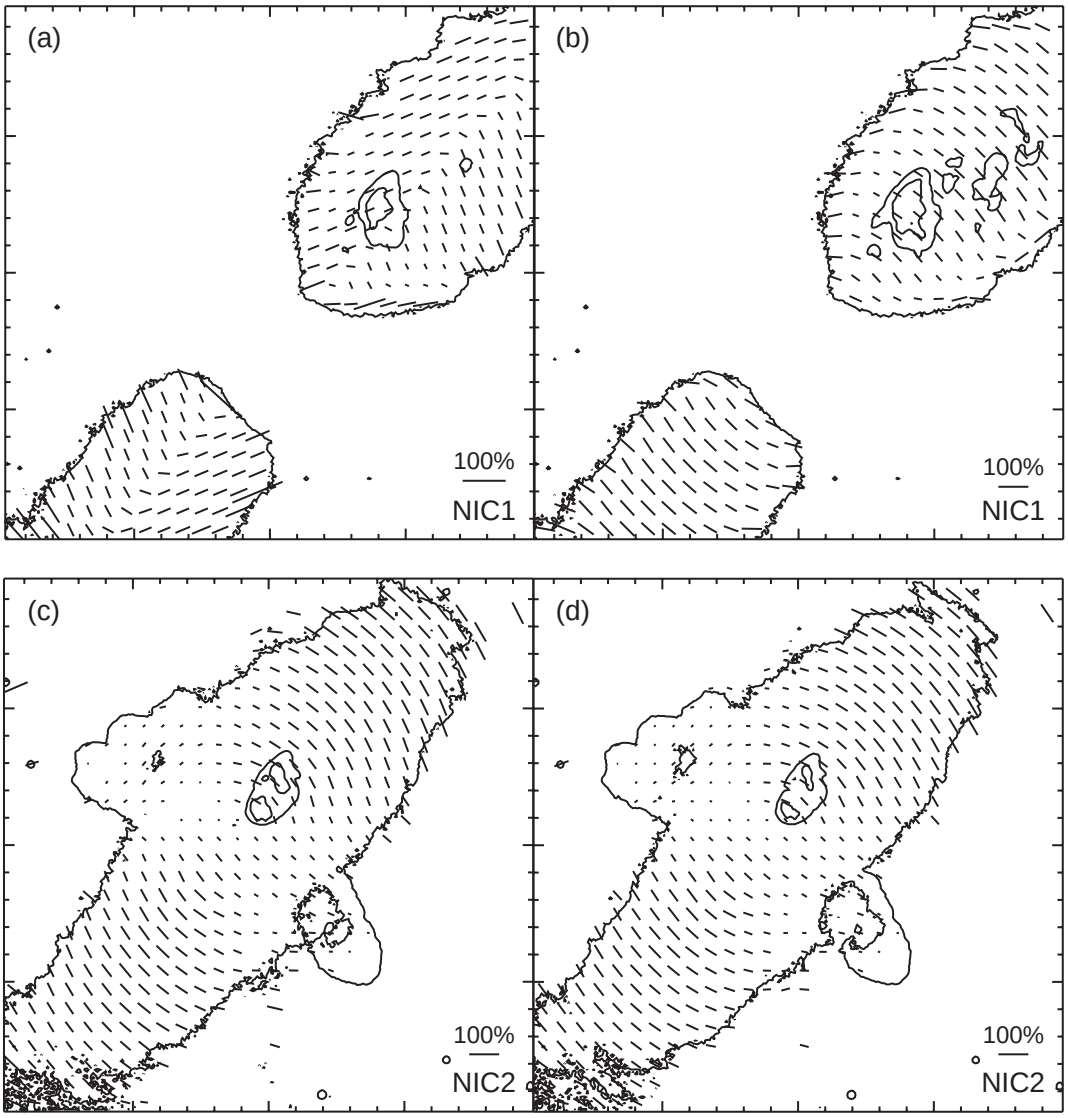

FIG. 7.—Comparison between the standard theory (*left panels*) and HSL (*right panels*) reduction methods. The data are for CRL 2688 observed with (*a*, *b*) NIC1 and (*c*, *d*) NIC2. The length of the 100% pseudovectors are indicated in each panel. Note that the 100% pseudovector in (*a*) is somewhat longer, owing to the expanded range needed to show clearly the lower (incorrect) polarizations that result from applying the standard method. For clarity, the polarizations have been binned by 9 × 9 pixels (in *q*, *u*). All panels show 256 × 256 pixels with 0.″04344 × 0.″04326 pixel^{-1} and 0.″07641 × 0.″07573 pixel^{-1} in NIC1 and NIC2, respectively. Geometric rectification has not been applied to these images (see text).

multiple-polarizer techniques is presented in the following section.

6. ERROR ANALYSIS OF NICMOS POLARIMETRY

Because of the idiosyncrasies of the three-polarizer filter sets (Table 1) and noise sources which include the detected photons, read noise, dark emission, and flat-fielding errors, we have chosen to evaluate the uncertainty distributions for NICMOS polarimetry using Monte Carlo methods. The procedure is straightforward: for each set of assumed parameters—spacecraft camera, object brightness, exposure time, degree and position angle of polarization—the number of detected photons was computed for each polarizer using equation (1). If this three-measurement "parent mean" were reduced using our algorithm, the input polarization and position angle would be recovered. Instead, a Monte Carlo approach was taken wherein a large number (typically 10^4–10^5 per parameter set) of "sample" measurements were generated by applying multiplicative and additive random noise components to the individual measurements with Poisson or Gaussian deviates of the appropriate dispersions. Each sample was then run through the reduction algorithm to yield distributions of "measured" $q = Q/I$ and $u = U/I$.

Polarizer characteristics were taken from Table 1. Detector parameters have been reported in Calzetti & Noll (1998) and Thompson et al. (1998); updated on-orbit values are presented here in Table 4. Because the total background count rate (detector dark current plus telescope and celestial background) is small ($\lesssim 1\ e^-$ pixel^{-1} s^{-1}), dark noise is dwarfed by other noise sources over the vast majority of parameter space. Therefore, exposure time is not an important variable. The uncertainty distributions are dominated by photon and read-noise contributions, scaled by the individual polarizer coefficients $\epsilon_k B_k$ and $\epsilon_k C_k$. Examples are provided in Figure 8 for six polarization position angle settings[8] 0°–150°, for the NIC1 (*left panel*) and NIC2 (*right panel*) polarizers. Each panel is a contour plot of the probability distribution of (q, u) which results from the simulation, computed per detector pixel for a completely polarized source and an assumed 1000 photons incident on each polarizing filter.

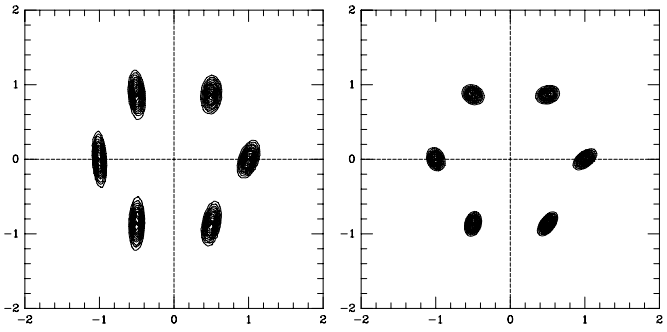

FIG. 8.—(*Left*) Probability distributions of polarization for the NIC1 camera and POLS filter set. Monte Carlo simulations depict the distributions of normalized Stokes parameters q (abscissa) and u (ordinate) for input polarization position angles $\theta = 0°$–150° in increments of 30°. $\theta = 0°$ lies along the $+x$-axis. A total of 1000 incident photons is assumed in each case. The asymmetric error distributions result from the use of three polarizers with nonstandard orientations and different transmissions and polarizing efficiencies (see Table 1). (*Right*) As for the left panel, representing the NIC2 camera and POLL filter set.

[8] $+q$ is aligned with $\theta = 0°$, as described in Table 1.

Because the polarimetric transformations are linear, the reduced Stokes parameter distributions are symmetric ellipses, and the means, $\langle q \rangle$ and $\langle u \rangle$, reproduce the input polarization values. At a given position angle, the error ellipse retains a constant shape but varies in size as a function of the photon number. The elliptical probability distributions result from a combination of two effects. First, measurement of a source with varying brightness (e.g., a polarized source observed through a rotating linear polarizer) will yield a varying relative precision when subjected to Poisson noise. This produces an ellipticity which scales with the degree of polarization of the source, moderated by the effects of other noise sources (dark emission and flat-field errors). Figure 9 illustrates the point for an assumed ideal set of three polarizers. Even in this case of

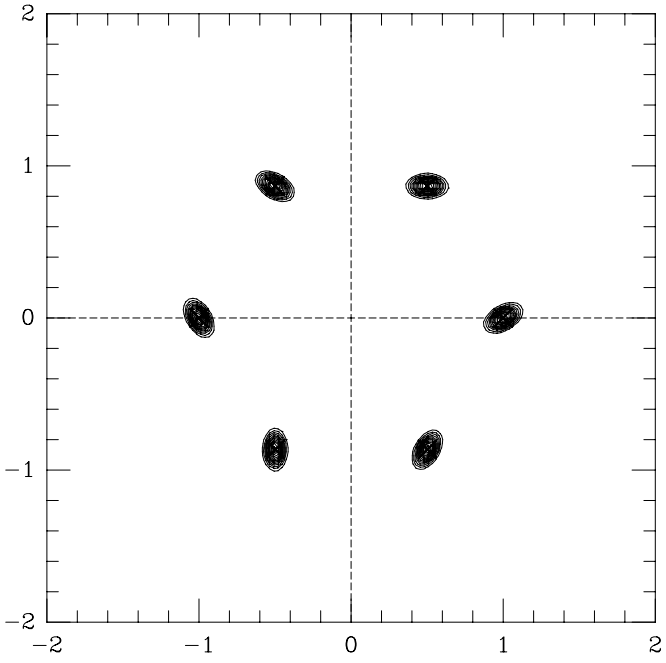

FIG. 9.—As for Fig. 8, assuming an "ideal" three-polarizer filter set, where all polarizers have unity efficiency and transmission and are oriented at 120° intervals. Note that the error ellipses are identical in shape and merely rotate with the input position angle of polarization.

TABLE 4

REVISED, ON-ORBIT NICMOS DETECTOR CHARACTERISTICS

	NIC1	NIC2
Gain (e^- ADU^{-1})	5.4	5.4
Read noise[a] (e^-)	22.0	29.0
Dark current (e^- s^{-1} pixel^{-1})	0.16	0.15
Telescope and celestial background (e^- s^{-1} pixel^{-1})	0.026	1.57
Flat-field accuracy (%)	0.3	0.3

[a] Read noise for typical MULTIACCUM sequence.

unity polarizing efficiency and 120° separations, the uncertainty distributions are not circular in (q, u) space and rotate with the polarization incoming position angle. Second, and more important for the typically low values of polarization encountered in nature, is the lack of symmetry imparted by unequal transmissions, polarizing efficiencies, and/or nonstandard orientations of the (NICMOS) polarizers. This results in one Stokes parameter being "better sampled" than the other, depending on the input polarization position angle, and resulting uncertainty distributions which differ markedly for q and u. This point underscores the problems of "debiasing" the polarization degree and position angle estimates formed from q and u (e.g., Simmons & Stewart 1985) and is a primary driver for the debiasing technique developed by Sparks & Axon (1999).

In Figure 10 we summarize the run of position angle–averaged $\langle\sigma_q\rangle$ and $\langle\sigma_u\rangle$ for the two NICMOS cameras. The dominant variable is the photon flux, here characterized by the number of photons which would be detected in a given exposure *in the absence of a polarizing filter*. In this way, the transmittance differences of the polarizers are reflected in the plotted results. The shapes of the curves can be understood intuitively by considering three regimes:

1. At very low light levels, where the photon count per exposure $N \lesssim 10^3$, read noise dominates and the uncertainty in a measured signal σ_S is largely independent of S. Since a Stokes parameter is basically the difference of signals divided by their sum, the uncertainty in q or u is proportional to the read noise divided by the light level. Hence $\sigma_{q,u} \propto N^{-1}$ near the left edge of Figure 10.

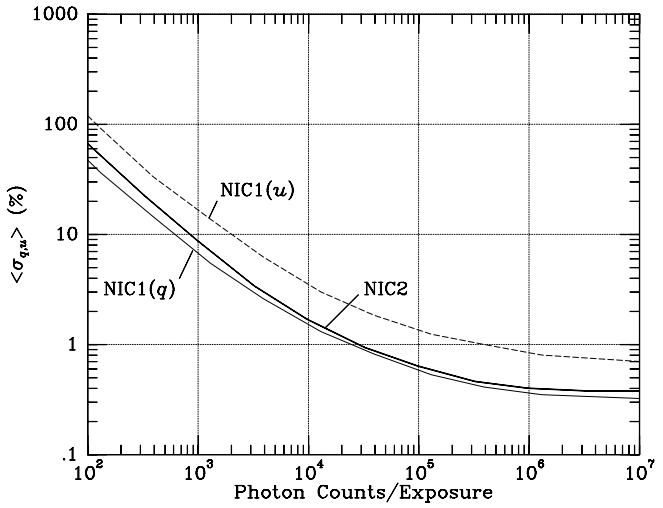

FIG. 10.—Monte Carlo results for the linear Stokes parameters of the NICMOS cameras. The position angle–averaged rms deviations in q and u are parameterized as functions of the number of photon counts pixel^{-1} exposure^{-1}, with exposure time being a very minor additional variable. The curves representing $\langle\sigma_q\rangle$ and $\langle\sigma_u\rangle$ for the NIC2 camera are almost indistinguishable at this scale. See text for details.

2. In the intermediate, photon noise–dominated regime, $10^3 \lesssim N \lesssim 10^5$, $\sigma_S \propto \sqrt{N}$, so $\sigma_{q,u} \propto N^{-0.5}$.

3. Finally, at very high photon levels, $N \gtrsim 10^5$ per pixel, photon noise is a small factor and the curve asymptotically approaches a limit dictated by the precision of flat-field division. This basic curve is shifted vertically by the polarizer efficiencies, which effectively transform measured signal differences into true Stokes parameters. For the NIC1 camera, the reduced efficiencies of the two filters which sample u (POL120S and POL240S) cause a systematic elongation of the error ellipses in that dimension and displacement of the $\langle\sigma_u\rangle$ curve in Figure 10 by more than a factor of 2.

Sparks & Axon (1999) have made a similar analysis of the three-polarizer case with both the ideal and real NICMOS NIC1 system, but assuming uniform Gaussian or Poisson noise distribution (i.e., no detector characteristics were included), corresponding to our photon noise–dominated regime. They too find that the nonideal nature of the NIC1 polarizers results in a factor of 2 degradation in performance compared to the ideal case.

For completeness, we present in the two panels of Figure 11 the error distributions for the single-detector, four-position sequence of the WFPC2 polarizer quad and for an ideal set of four polarizers. In the case of four polarizers, the variables I, Q, and U in equation (1) are overdetermined and best solved for by least squares. Indeed, the $n \geq 3$ polarizer case can be expressed as an equivalent set of three-polarizer observations (Sparks & Axon 1999). However, using more than three polarizers allows better sampling of (q, u) space. Because of this, identical polarizers at 45° increments yield error distributions that are circular regardless of input position angle. The polarizing efficiency of the WFPC2 polarizer is nearly ideal ($\epsilon = 0.96$ at $\lambda = 4400$ Å; Biretta 1996; Biretta & McMaster 1997); however, the "partial-rotation" technique used to generate the POLQ,

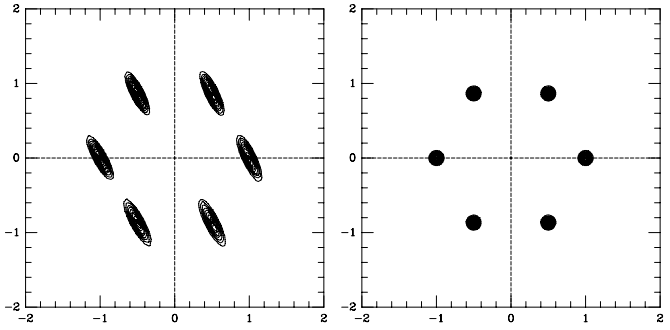

FIG. 11.—(*Left*) As for Fig. 8, but assuming the single-polarizer, four-position "partial-rotation" mode of the polarizer quad filter of WFPC2 ($\lambda = 4400$ Å). (*Right*) The ideal four-polarizer filter set. Note that in this case, the error distributions in (q, u) space are circles.

POLQN33, POLQP15, and POLQN18 orientations cluster near an axis inclined $\sim 20^\circ$ from q, so the error distributions are highly elongated in the direction orthogonal to that on a (q, u) plot.

7. TIPS FOR OPTIMUM PERFORMANCE

The NICMOS Instrument Handbook (Calzetti et al. 1999) provides good general guidelines for observing with NICMOS. However, a few words of advice are appropriate.

Since image persistence may arise in some NICMOS images, consecutive observations in different polarizers should not be obtained without moving the object on the array. For example, if the object is not moved between POL0S and POL120S, persistent signal could appear in POL120S, and the resulting polarization measurement may be compromised. A spiral-dither pattern in each polarizer with half-integer offsets will minimize persistence, improve sampling, and ensure that important structure is not lost to a bad pixel.

To avoid the image ghosts which affect the very low light level polarimetric performance of NIC1 in the presence of strong point sources (Figs. 3 and 4), observations at multiple epochs, using different orientations of the spacecraft, can be combined to "fill in" areas that are obliterated by the ghosts. While this will not allow the removal of ghosts images from affected frames, it should enable recovery of polarization information across the entire field of view for objects which do not vary.

As noted for CRL 2688 (the Egg Nebula), images should be rectified to project square pixels on the sky. While the degree of polarization and position angle per pixel are accurately determined by the HSL algorithm in the observed image, the relative locations of pixels, and thus the position angle structure in the object, will be skewed in unrectified images.

Guidance in estimating necessary integration times to obtain desired polarimetric accuracies can be gleaned from our error analysis and that of Sparks & Axon (1999). In particular, the error in the degree of polarization (σ_p) can be estimated from the inverse of the average signal-to-noise ratio per polarizer image in the photon noise–dominated regime (Fig. 10 and Sparks & Axon 1999) and multiplied by ~ 2 for NIC1. Since the NIC2 polarizers are more nearly ideal, $\sigma_p \sim \sqrt{2/N}$ in the photon-dominated regime. Although debiasing techniques like that of Sparks & Axon (1999) can be used to estimate the degree of polarization for $p/\sigma_p \gtrsim 1$, in general we strongly urge potential observers to design their experiments to achieve $p/\sigma_p > 4$. At these detection levels, the polarization results will be less susceptible to the details of the error distribution and debiasing procedures used.

We have shown that NICMOS is capable of producing highly accurate imaging polarimetry from 1–2 μm to a spatial resolution of a few tenths of an arcsecond when the data are reduced appropriately. The superior resolution, dynamic range, and stability of the *HST*/NICMOS system allows unprecedented detail in investigations of the near-IR polarization properties of a wide variety of objects. Cycle 7 GTO and GO programs addressed topics from the nature of active galactic nuclei, to protoplanetary nebula, to embedded young stellar objects, to planetary surfaces. With the anticipated refurbishment in 2001, the NICMOS system will continue provide a truly unique and powerful tool for the study of polarized light.

It is a pleasure to thank B. Stobie, H. Chen, L. Bergeron, and A. Evans for assistance with the (nonpolarimetric) data calibration. Thanks to D. Axon, D. Daou, D. Gilmore, and L. Colina for their planning of the STScI calibrations. We also benefited from discussions with W. Sparks and E. Young. We thank R. Thompson (Project PI), M. Rieke (Deputy PI), and the members of the NICMOS Instrument Definition Team (IDT) for their effort in building such a fine instrument. We thank E. Mentzell for assistance understanding the NICMOS optical prescription and definition of axes. Finally, special thanks go to J. Kastner for the use of his COB observations, to R. Sahai for the NIC1 polarimetry of CRL 2688, and to Eric Ramberg at Ball Aerospace for details on the construction and mounting of the POLS filter sets. We also acknowledge the anonymous referee for helping us to clarify several points which improved the manuscript. This work is supported by NASA grant NAG 5-3042 to the NICMOS IDT. The NICMOS images were obtained with the *Hubble Space Telescope*, which is administered by the Space Telescope Science Institute, which is operated by Association of Universities for Research in Astronomy, Incorporated, under NASA contract NAS 5-26555.

REFERENCES

Axon, D., et al. 1996, NICMOS Instrument Handbook Version 1.0 (Baltimore: STScI)
Biretta, J., ed. 1996, Wide Field and Planetary Camera 2 Instrument Handbook, Version 4.0 (Baltimore: STScI)
Biretta, J., & McMaster, M. 1997, Instrument Science Report WFPC2-97-011 (Baltimore: STScI)
Bobrowsky, M., Meixner, M., Axon, D., Hines, D. C., & Skinner, C. 2000, AJ, in preparation
Calzetti, D., et al. 1999, NICMOS Instrument Handbook, Version 3.0 (Baltimore: STScI)
Calzetti, D., & Noll, K. 1998, Instrument Science Report NICMOS-98-014 (Baltimore: STScI)

Dickinson, M. et al. 1999, NICMOS Data Handbook, Version 4.0 (Baltimore: STScI)
Hines, D. C. 1998, in NICMOS and the VLT: A New Era of High Resolution Near Infrared Imaging and Spectroscopy, ESO Conf. & Workshop Proc. 55, ed. W. Freudling & R. Hook (Garching: ESO), 63
Hines, D. C., Schmidt, G. D., & Lytle, D. 1997, in The 1997 *HST* Calibration Workshop, ed. S. Casertano et al. (Baltimore: STScI) [HSL97]
Kastner, J., & Weintraub, D. 1994, ApJ, 434, 719
Mazzuca, L., & Hines, D. C. 1999, Instrument Science Report NICMOS-ISR-99-004 (Baltimore: STScI)
Mazzuca, L., Sparks, B., & Axon, D. 1998, Instrument Science Report NICMOS-ISR-98-017 (Baltimore: STScI)
Miller, J. S., Robinson, L. B., & Goodrich, R. W. 1988, in Proc. 9th Santa Cruz Summer Workshop, Instrumentation for Ground-based Optical Astronomy, ed. L. B. Robinson (New York: Springer), 157
Sahai, R., Hines, D. C., Kastner, J. H., Weintraub, D. A., Trauger, J. T., Rieke, M. J., Thompson, R. I., & Schneider, G. 1998, ApJ, 492, L163
Schmidt, G. D., Elston, R., & Lupie, O. L. 1992, AJ, 104, 1563
Schmidt, G. D., Stockman, H. S., & Smith, P. S. 1992, ApJ, 398, L57
Serkowski, K. 1974, Methods of Experimental Physics 12A, Optical and Infrared, ed. N. Carleton (New York: Academic), 361
Simmons, J. F. L., & Stewart, B. G. 1985, A&A, 142, 100
Sparks, W. B., & Axon, D. J. 1999, PASP, 111, 1298
Thompson, R. I., Rieke, M., Schneider, G., Hines, D. C., & Corbin, M. R. 1998, ApJ, 492, L95
Weintraub, D., Kastner, J., Hines, D. C., & Sahai, R. 2000, ApJ, 531, 401
Whittet, D. C. B., Martin, P. G., Hough, J. H., Rouse, M. F., Bailey, J. A., & Axon, D. J. 1992, ApJ, 386, 562